RESEARCH ARTICLE

Flow characteristics and dynamic responses of a parked straight-bladed vertical axis wind turbine

Limin Kuang[1] | Jie Su[1] | Yaoran Chen[1] | Zhaolong Han[1,2] (iD) | Dai Zhou[1,2,3,4] |
Yongsheng Zhao[1,2] | Zhiyu Jiang[5] (iD) | Yan Bao[1]

[1]School of Naval Architecture, Ocean and Civil Engineering, Shanghai Jiao Tong University, Shanghai, China

[2]State Key Laboratory of Ocean Engineering, Shanghai Jiao Tong University, Shanghai, China

[3]Key Laboratory of Hydrodynamics of Ministry of Education, Minhang Campus, Shanghai, China

[4]Collaborative Innovation Center for Advanced Ship and Deep-Sea Exploration (CISSE), Shanghai, China

[5]Department of Engineering Sciences, University of Agder, Grimstad, Norway

Correspondence
Zhaolong Han and Dai Zhou, School of Naval Architecture, Ocean and Civil Engineering, Shanghai Jiao Tong University, Shanghai 200240, China.
Emails: han.arkey@sjtu.edu.cn (ZH); zhoudai@sjtu.edu.cn (DZ)

Abstract

With the development of urbanization and the application of renewable energy, wind turbine is becoming an important approach for wind energy reservation and utilization. This study provides a numerical investigation on understanding the surface pressure distribution, flow characteristics and dynamic responses of a parked straight-bladed vertical axis wind turbine (VAWT), which is helpful for its design. Together with the two-way coupling method between simulation platforms such as STAR-CCM+ and ABAQUS, the SST k-ω turbulence model is used to obtain the surface pressure and surrounding flow of the VAWT, and the finite element method is used to obtain the dynamic responses of its structural components. The results show that the contours of the pressure distribution on the windward surface of the VAWT are similar even under a few different conditions, and the deformation of the VAWT can lead to changes in surface pressure; the turbulent flow characteristics and the wake effect become more obvious as the wind velocity increases; the blades and support arms of the VAWT need to be reinforced during the design, and the effect of the parked condition on the dynamic responses of the VAWT can be neglected. The two-way coupling method as well as the numerical simulation results is expected to provide references for the design of VAWTs subjected to coming wind action.

KEYWORDS
dynamic responses, flow characteristics, two-way coupling method, vertical axis wind turbine

1 | INTRODUCTION

With the depletion of fossil fuel resources, the energy issue has become a key factor affecting the sustainable development of

a country.[1] Therefore, countries around the world have made the development of renewable energy as an important strategic target. The renewable energy sources that researchers mainly concerned with include biomass, solar, geothermal,

hydroelectric, and wind.[2] Among them, wind energy has the advantages of clean and pollution-free, wide distribution range and large reserves, hence has been gradually becoming one of the most important choices for countries to develop and utilize renewable energy. As a wind energy conversion equipment, wind turbines have been continuously improved and widely used.

According to the position of the rotating shaft, wind turbines can be classified into horizontal axis wind turbine (HAWT) and vertical axis wind turbine (VAWT).[3,4] Due to the higher wind energy conversion efficiency of HAWTs, they have been the focus of researchers for the past few decades.[5,6] However, with the rapid development of urbanization and relying on unique advantages, VAWTs have obtained increasing attention recently. Compared with HAWTs, the following characteristics of VAWTs are found to be more suitable for urban areas where winds are unsteady and gusty.[2,7-10]

1. VAWTs can capture incoming wind from any direction without yaw mechanisms, which reduces design and manufacturing costs.
2. The inertial and gravity forces of VAWTs remain unchanged, and the load on the wind turbine is relatively constant, helping to reduce structural vibration and fatigue damage.
3. VAWTs produce less aerodynamic noise and have better performance in turbulent wind conditions.

Vertical axis wind turbines can mainly be divided into Darrieus type, Savonius type, and Giromill type.[11] Among them, the Darrieus-type wind turbines can convert the highest amount of energy due to a higher tip-speed ratio.[12] The straight-bladed VAWTs developed from traditional Darrieus-type wind turbines have simple blade shapes and wind wheel structures, which are convenient to design and install. Besides, for numerical modeling, the regular blade shapes can reduce the workload and computational cost during the simulation process.

Although VAWTs have broad application prospects in urban areas, structural safety still restricts their further development. The support towers of VAWTs are usually slender and are susceptible to wind loads, especially in areas with strong winds. Such a characteristic poses great challenges to the normal operation of wind turbine systems. In urban areas with dense traffic, damaged wind turbines can also pose a safety hazard to pedestrians. Therefore, more and more attention has been paid to the dynamic responses of wind turbines under wind loads, both experimentally and numerically.

Several laboratory vibration tests were conducted to study the dynamic behavior of VAWTs. Wang et al[12] investigated the ambient dynamic responses of a rooftop VAWT and found

that the wind direction has little effect on its vibration amplitude. Mclaren et al[13] showed that the vibration of the VAWT support tower may be influenced by the wind turbine's operation. Nowadays, the finite element method is widely used to analyze the dynamic responses of VAWTs numerically.[14] Rebelo et al[15] used a numerical model of support tower setup by finite element technique to compare with the measurement results and verified its feasibility. Avila et al[16] solved the vibration equation of a wind turbine tower and got a valuable result. Li et al[17] analyzed the dynamic behaviors of a VAWT and discovered that the influence of gyroscopic moment on the dynamic characteristics of the support tower during the rotation can be ignored. Feliciano et al[18] demonstrated that the mass imbalance due to the rotational effect of the blades has a minor effect on the tower deflection through finite element analysis (FEA). However, so far, there are still many problems that need to be further analyzed and solved. For example, Avila et al[16] simplified the wind action to a concentrated load, which affected the creditability of the computational results. And the dynamic responses of the wind turbine under different wind loads are rather different, which were not considered in the research of Li et al[17] In addition, most of the existing researches mainly focus on the dynamic responses of the wind turbine support tower, while the researches on other structures such as blades and support arms are relatively few. However, the damage probability of the blades and support arms is much higher than the support tower, which deserves more attention.[19] On the other hand, in the above studies, the characteristics of flow around the wind turbine have not been described, which may have important influence on dynamic behaviors of the wind turbine structural system.

Computational fluid dynamics (CFD) method can describe the loading process of wind to structure more accurately and overcome some limitations of wind tunnel tests such as high cost and complex test environment.[20] It is often utilized in the studies of aerodynamic performance of wind turbines, however, rarely be used in dynamic responses analysis.[21] Hence, in order to simulate the flow around the wind turbine and better reflect the wind loads, the two-way coupling method combining the CFD prediction and FEA technique is proposed.

The main work of the present study is to analyze the surface pressure distribution, flow characteristics, and dynamic responses of a straight-bladed VAWT under different steady wind conditions, using the two-way coupling method. Compared with HAWTs, since the wind direction and operating state have relatively small influence on the vibration of straight-bladed VAWTs,[12,18,22] and in order to reduce the workload of the numerical simulation, only the parked conditions of the VAWT at different rotation angles are considered. The following points make this study different from previous ones: (a) the two-way coupling method is adopted; (b) the dynamic responses of the whole structural system of the VAWT

including the blades and support arms are calculated; (c) the variations of the flow around the VAWT under different wind conditions are revealed; (d) the effects of different parked conditions on the surface pressure distribution, flow characteristics, and dynamic responses of the VAWT are analyzed.

The structure of this paper is organized as follows: Section 2 presents the specific numerical simulation methods adopted in this study; the validation of the two-way coupling method is provided in Section 3; in Section 4, the VAWT model for analysis is described and the results are discussed in Section 5; finally, several concluding remarks are made in Section 6.

2 | NUMERICAL SIMULATION METHOD

Under the commercial CFD platform STAR-CCM+, the SST k-ω turbulence model is used to obtain the surface pressure and surrounding flow of the VAWT in different steady wind conditions and different parked conditions. The time-domain dynamic responses of the VAWT are calculated by the finite element software ABAQUS, using the traction loads extracted from STAR-CCM+. The two-way coupling procedure between the two solvers is reached through an iterative process to obtain a full solution by means of exchanging results information through the fluid-structure interface. The specific simulation methods are shown in the following sections.

2.1 | Computational fluid dynamics

The CFD simulation methods of turbulence mainly include direct numerical simulation (DNS), large eddy simulation (LES), detached eddy simulation (DES), and Reynolds-averaged Navier-Stokes (RANS) method.[5] Compared with other three methods, RANS method takes less computational cost

and can still produce satisfying results. Among RANS models, the SST k-ω turbulence model proposed by Menter[23] is found to have good prediction in the simulation of straight-bladed VAWTs, as verified by Ma et al[5] Therefore, it is chosen in the present study. In SST k-ω turbulence model, the k and ω equations can be expressed as

$$\frac{\partial}{\partial t}(\rho k) + \frac{\partial}{\partial x_j}(\rho k u_i) = \frac{\partial}{\partial x_j}\left[\Gamma_k \frac{\partial k}{\partial x_j}\right] + G_k - Y_k \quad (1)$$

$$\frac{\partial}{\partial t}(\rho \omega) + \frac{\partial}{\partial x_j}(\rho \omega u_j) = \frac{\partial}{\partial x_j}\left[\Gamma_\omega \frac{\partial \omega}{\partial x_j}\right] + G_\omega - Y_\omega + D_\omega \quad (2)$$

where ρ, k, ω, u_i (u_j), and t are the density, turbulent kinetic energy, turbulent dissipation rate, velocity, and time, respectively. Γ_k, G_k, and Y_k are the convection term, production, and effective diffusion term of k, respectively. Γ_ω, G_ω, Y_ω, and D_ω are the convection term, production, effective diffusion term, and cross-convection term of ω, respectively.

2.2 | Dynamic responses by finite element analysis

A VAWT is like a vertical cantilever structure. When calculating its dynamic responses, the kinetic equation is given as

$$[M]\{\ddot{x}(t)\} + [C]\{\dot{x}(t)\} + [K]\{x(t)\} = \{F(t)\} \quad (3)$$

where $\{\ddot{x}(t)\}$, $\{\dot{x}(t)\}$, and $\{x(t)\}$ are acceleration, velocity, and displacement vectors, respectively. $[M]$, $[C]$, and $[K]$ are mass, damping, and stiffness matrices, respectively. $\{F(t)\}$ is the wind load extracted from STAR-CCM+. Afterward, the implicit dynamic algorithm of Newmark method[24] is
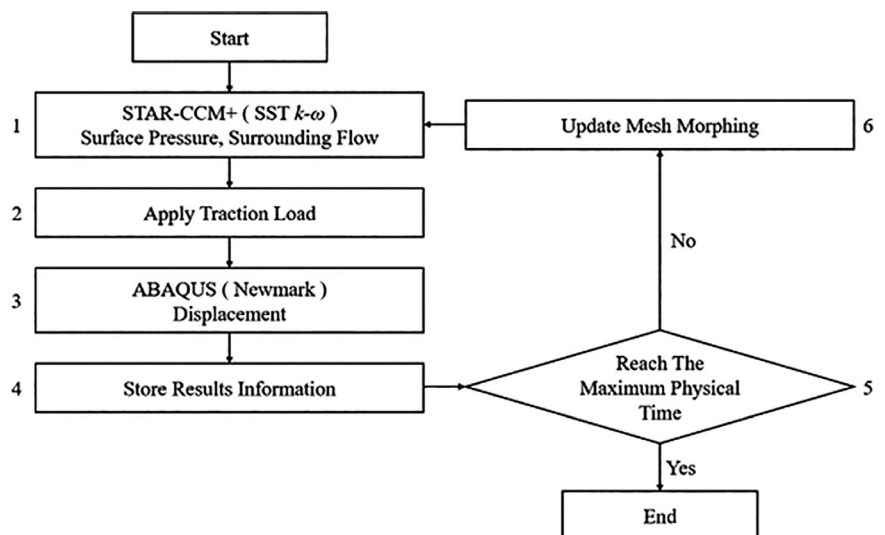

FIGURE 1 Flowchart illustrating the two-way coupling between STAR-CCM+ and ABAQUS

TABLE 1 Oscillating plate model parameters

Parameter	Value
Length	400 mm
Width	10 mm
Height	1000 mm
Young's modulus	$3.5e9 \text{ N/m}^2$
Poisson's ratio	0.32
Density	1200 kg/m^3

chosen to obtain the dynamic responses of the VAWT in ABAQUS.

2.3 | Two-way coupling procedure

The algorithm describing the two-way coupling procedure between STAR-CCM+ and ABAQUS is featured in Figure 1. First, the surface pressure and surrounding flow of the VAWT are obtained from STAR-CCM+ with SST k-ω turbulence model (step 1). Then, the traction loads are applied to the finite element model in ABAQUS, to simulate dynamic responses of the VAWT in an iterative way (steps 2 and 3). Afterward, the displacements are sent back to STAR-CCM+ to update the mesh morphing (step 6). The results information is exchanged at frequent intervals until the maximum physical time is reached (step 5). For every

circular simulation, the results are stored in step 4 for further analysis.

3 | VALIDATION OF THE TWO-WAY COUPLING METHOD

In this section, the oscillating plate model from the research conducted by Glück et al[25] is used to verify the feasibility and accuracy of the two-way coupling method. In this research, the dynamic behaviors of a vertical plate under a steady fluid flow are analyzed by CFD-CSD method. The sizes and mechanical properties of the plate are shown in Table 1, and the bottom of the plate is fixed. The fluid has a density of 1 kg/m^3, and its dynamic viscosity is 0.2 Pa s. The computational model constructed in STAR-CCM+ and ABAQUS is shown in Figure 2. The length, width, and height of the computational domain are 6000 mm, 6000 mm, and 2000 mm, respectively, as shown in Figure 2A. In order to be consistent with the settings of the VAWT numerical simulation, the unstructured trimmed cells with varied sizes are adopted in this validation (Figure 2B,C), and there are roughly 600 000 grids in the whole computational domain. The C3D8R element is used in ABAQUS to generate a total of 32 000 grids as shown in Figure 2D. The inlet velocity is 10 m/s, and the outlet pressure is 0.0 Pa. The total simulation time is 2.5 seconds, and the constant coupling time step

(A)

(B)

(C)

(D)
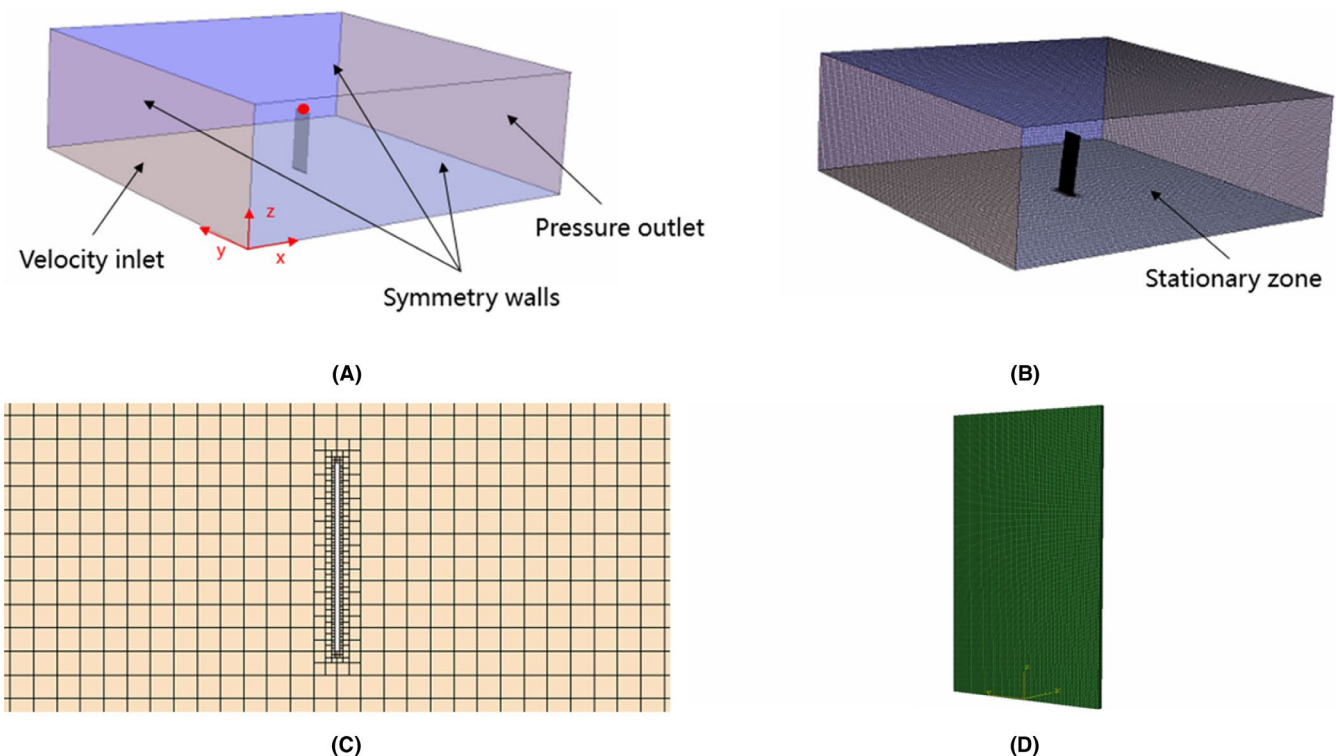
FIGURE 2 Computational model: A, computational domain; B, over view of the grids; C, grids around the plate; D, 3D view of the finite element model

is 0.01 seconds. The displacement of the free edge of the plate in the *x*-direction is selected as the comparison object, and the specific position is indicated by a red point which is shown in Figure 2A.

The numerical results of the validation are shown in Figure 3, and the two-way coupling simulation results fit well with those of the literature.[25] The vibration amplitude and frequency of the oscillating plate are basically coincident under the two computation conditions. Hence, the two-way coupling method can accurately predict the dynamic behaviors of the vertical plate, which can be used in subsequent computations of the VAWT.

4 | NUMERICAL MODEL

To start up a two-way coupling simulation, separate numerical models are prepared in STAR-CCM+ and ABAQUS, respectively. The boundary conditions and physics models are defined in STAR-CCM+, and the material properties are set up in ABAQUS. The specific numerical models are given in the following sections.

4.1 | Wind turbine model

A straight-bladed VAWT is selected as the research object in this study. Its three-dimensional (3D) model is built in the structural design software Unigraphics NX as shown in Figure 4A and then is import into STAR-CCM+ and ABAQUS for numerical simulation. The major structural components of this model include blades, support arms, and support tower. The airfoil section of the blades is NACA0021 airfoil with a chord length of $c = 925.6$ mm (Figure 4B). The blade span is $h = 6300$ mm, and the pitching angle is $\beta = 8°$. The support tower consists of two

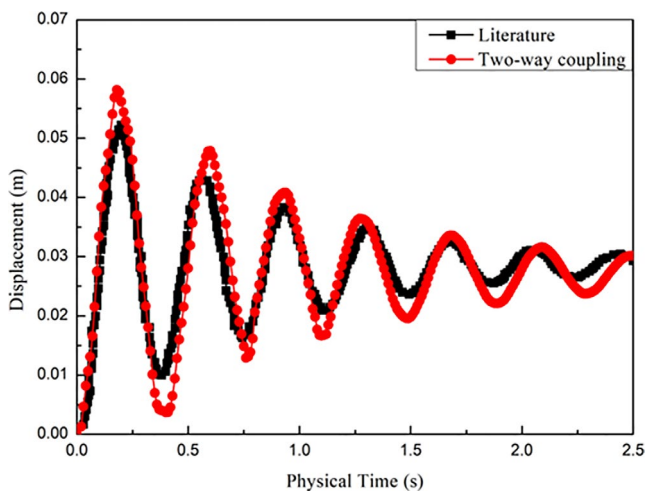**FIGURE 3** Validation of the two-way coupling method between the simulation and literature[25]

shafts with different diameters. The lower part has a diameter of $d_1 = 650$ mm and a height of $H_1 = 5400$ mm. The upper part has a diameter of $d_2 = 700$ mm and a height of $H_2 = 4200$ mm. The junction of the two parts is defined as the variable section (Figure 4A). The support arms are $d_3 = 200$ mm in diameter, and the diameter of the rotor is $D = 7000$ mm (Figure 4B).

In this study, the parked conditions of the VAWT at three different rotation angles are investigated. According to the relative position of the blades and the support tower, and considering the periodicity during the rotation of the three-blade wind turbine system, the state when the angle between blade 1 and *y*-axis is $\theta = 0°$ (Figure 4B) is taken as the first parked condition, and the angles of 90° and 135° are set as the second and third parked conditions, respectively (Figure 4C,D).

4.2 | Computational fluid dynamics model

An appropriate 3D computational domain is constructed in STAR-CCM+ as shown in Figure 5A. The first parked condition is used to indicate the specific situation. As the current study considers the parked conditions of the VAWT, the computational domain only contains the stationary zone and a block is set to improve the accuracy of the simulation. Considering the wake generation and flow field blocking rate requirements, the length, width, and height of the computational domain are 70 000 mm, 30 000 mm, and 20 000 mm, respectively, as shown in Figure 5B,C. The types of the inlet and outlet are set as velocity inlet ($V_1 = 5$ m/s, $V_2 = 10$ m/s, and $V_3 = 20$ m/s) and pressure outlet ($P = 0.0$ Pa), respectively. The freestream turbulence intensity is set as 1%. The surfaces of the VAWT and the bottom side of the stationary zone are set as no-slip walls. The other three sides of the stationary zone are set as symmetry walls.

The mesh topology is also completed in STAR-CCM+ with automatic meshing technique, and unstructured trimmed cells are generated in the computational domain as shown in Figure 6A. In order to investigate the flow characteristics of the VAWT, the mesh around the VAWT is refined as shown in Figure 6B. The boundary layer conditions of the support tower and blade are shown in Figure 6C,D. The prismatic boundary layer grids are set along the normal direction of the support tower and blades. The total thickness of the boundary layer is 0.00294 m with 30 layers and a growth ratio of 1.1. Based on the inlet velocity (5 m/s, 10 m/s and 20 m/s) and the chord length (0.9256 m), the Re (Reynolds number) of the present study is about 3.09e5-1.23e6. In order to meet the requirements of the SST k-ω turbulence model, the thickness of the first prismatic layer grid is set as 1.79e−5 which ensures $y^+ < 1$.

(A)

(B)   **(C)**   **(D)**
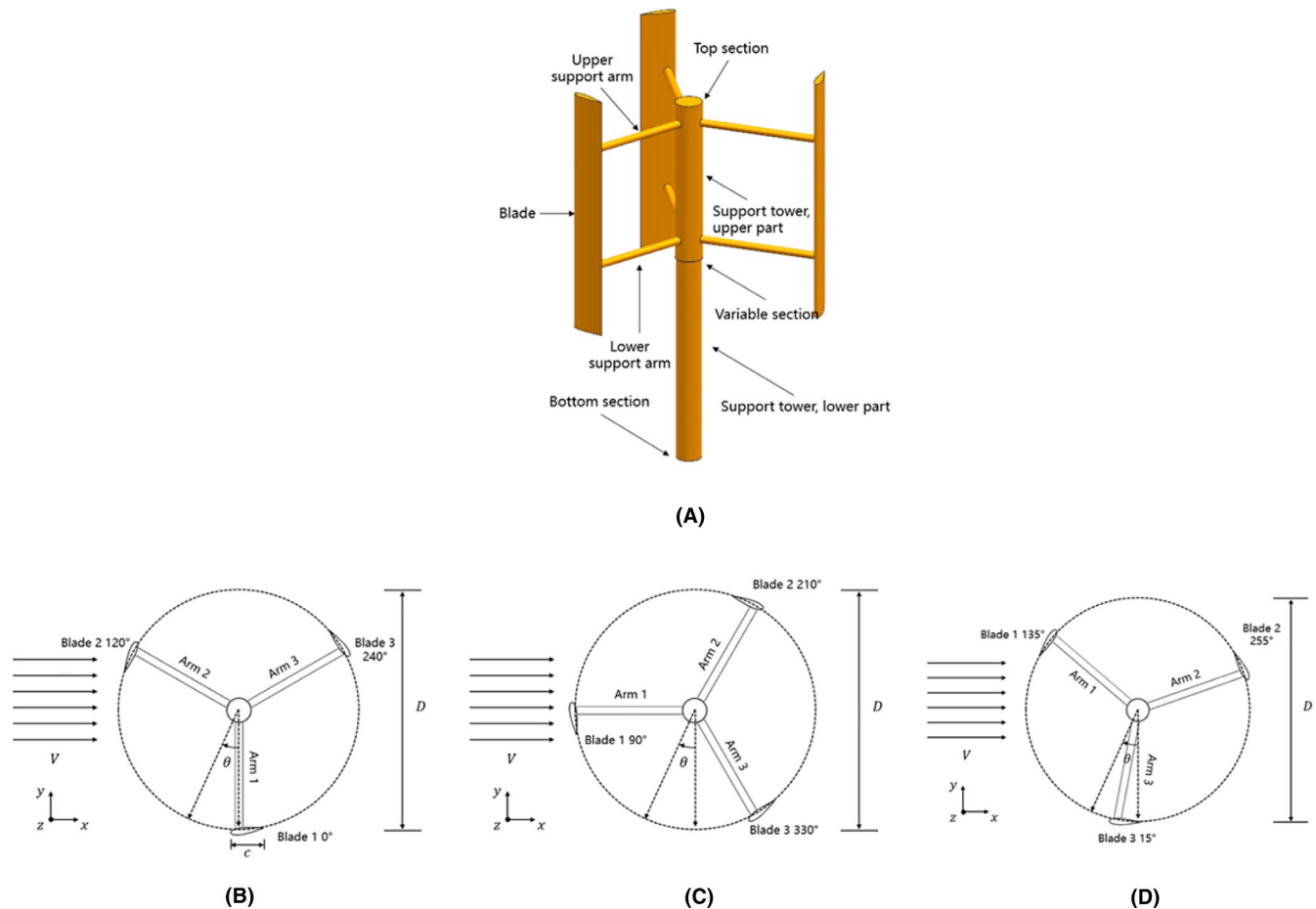
FIGURE 4 Straight-bladed VAWT model: A, 3D view; B, top view (the first parked condition, $\theta = 0°$); C, top view (the second parked condition, $\theta = 90°$); D, top view (the third parked condition, $\theta = 135°$)

4.3 | Finite element model

The finite element model of the VAWT is built in ABAQUS for two-way coupling as shown in Figure 7. The bottom of the VAWT support tower is fixed without displacement and rotation. Due to the difficulty of meshing the trailing edge of the blades and the support arm joints, the Tet (tetrahedral) element is utilized in the current study to divide the grid. The number of grids in the finite element model is basically consistent with the CFD model. The material of the support tower and support arms is steel, and its density and Young's modulus are set to 7850 kg/m^3 and 2.06e11 N/m^2, respectively. The blades are made with aluminum alloy, and its density and elastic modulus are taken as 2700 kg/m^3 and 7e10 N/m^2, respectively. The Poisson's ratio of the two materials is equal to 0.3.

4.4 | Mesh independence test

The mesh quantity and quality have an important impact on the computational accuracy and efficiency of the numerical simulation. Therefore, the mesh independence of the numerical model needs to be tested before the formal calculations. In the present mesh independence test, three types of mesh

topologies are considered and compared, which are called "Coarse," "Medium," and "Fine," respectively. Since the flow characteristics and wind-induced dynamic responses of the VAWT are mainly affected by the mesh quantity around the VAWT, the difference between the three types of mesh topologies is the grid density along the surfaces of the blades and support structure. The grid sizes of the blades and support structure are set to 0.1 m, 0.04 m, and 0.02 m in the three types of mesh topologies, respectively. In the first parked condition, the representative dynamic responses data of the top section ($z = 9.6$ m) and variable section ($z = 5.4$ m) of the VAWT support tower at the wind velocity of 10 m/s are selected as the comparison objects, including the maximum displacement, average displacement, and maximum velocity. The specific locations of the two sections are shown in Figure 4A. Due to lack of experimental data about the wind-induced dynamic responses, the computational results of the "Fine" mesh topology are taken as the reference for error relative calculation.

The results are shown in Tables 2 and 3. It can be seen that the "Coarse" mesh topology produces the largest relative error, approximately 20%, and its results are unreliable.
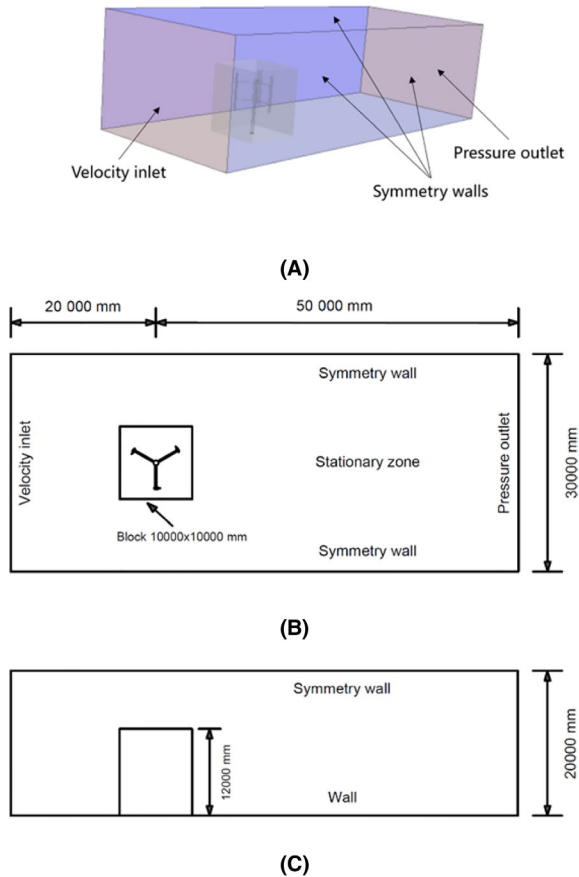
FIGURE 5 Computational domain and boundary conditions: A, 3D view; B, top view; C, front view

The computational results of the "Medium" and "Fine" mesh topologies are relatively close. However, a larger number of grids do not always mean more accurate results which it may affect the mesh quality, as verified by Lei et al[10] and Su et al[26] Therefore, considering the computational cost and accuracy, the "Medium" mesh topology is selected to accomplish the formal numerical simulation.

4.5 | Time step test

Time step test is also an important part to ensure reliability of numerical simulation results. Therefore, the current study sets three different time steps for comparison to assess the computational cost and precision, which are 0.05 seconds, 0.01 seconds, and 0.005 seconds, respectively. As with the mesh independence test, the representative dynamic responses data with the wind velocity of 10 m/s at critical sections of the VAWT support tower in the first parked condition are chosen as the comparison objects.

The results are shown in Tables 4 and 5. These are shown that the largest relative error occurs at the time step of 0.05 seconds and the peak reaches 30%. The results are nearly coincident when the time steps are 0.01 seconds and

0.005 seconds. Combining with the computational cost, the time step 0.01 seconds is selected for all simulations.

4.6 | Two-way coupling simulation setup

For each numerical model, a set of two-way coupling simulation parameters are specified. In STAR-CCM+, the VAWT makes up the fluid-structure interface. The pressure and wall shear stress are transmitted to ABAQUS with a constant coupling time step. In ABAQUS, the nodal displacement is sent back to STAR-CCM+ and the increment size of the implicit dynamic solution is consistent with the constant coupling time step to ensure the smooth progress of the two-way coupling simulation.

4.7 | Solver settings

For the simulation in STAR-CCM+, the second-order upwind scheme is selected for the discretization of convection terms and the diffusion terms discretization is accomplished with the second-order central-differencing scheme. The implicit unsteady segregated flow method is used for calculating discretization equations, and the AMG (algebraic multi-grid) technique combined with Gauss-Seidel iterative method is adopted. Meanwhile, the pressure-correction approach is utilized to solve the continuity and momentum equations. The coupling between the pressure-velocity equation and SST k-ω turbulence model is achieved with the SIMPLE algorithm. In the calculation of ABAQUS, the implicit dynamic algorithm of Newmark method is utilized to solve the kinetic equations of the VAWT.

The coupling time step is set as 0.01 seconds, and 10 iterations are set in one time step, which can achieve the convergence of the numerical simulation with less computational costs. Due to the good convergence performance in the above mesh independence test and time step test, the under-relaxation factor is consistent with the default setting of STAR-CCM+, which is taken as 0.8. All simulations are performed in parallel on a Small-Scale Server with two Intel (R) Xeon (R) CPUs (E5-2630 v3), and the calculation of one time step requires about 260 seconds.

5 | RESULTS AND DISCUSSION

Due to the large computational cost of the two-way coupling between STAR-CCM+ and ABAQUS, the results within 20 seconds are given in this study which can illustrate the surface pressure distribution, flow characteristics, and dynamic responses of the VAWT. The analysis is mainly for the first parked condition and the other two conditions are taken as comparison objects.
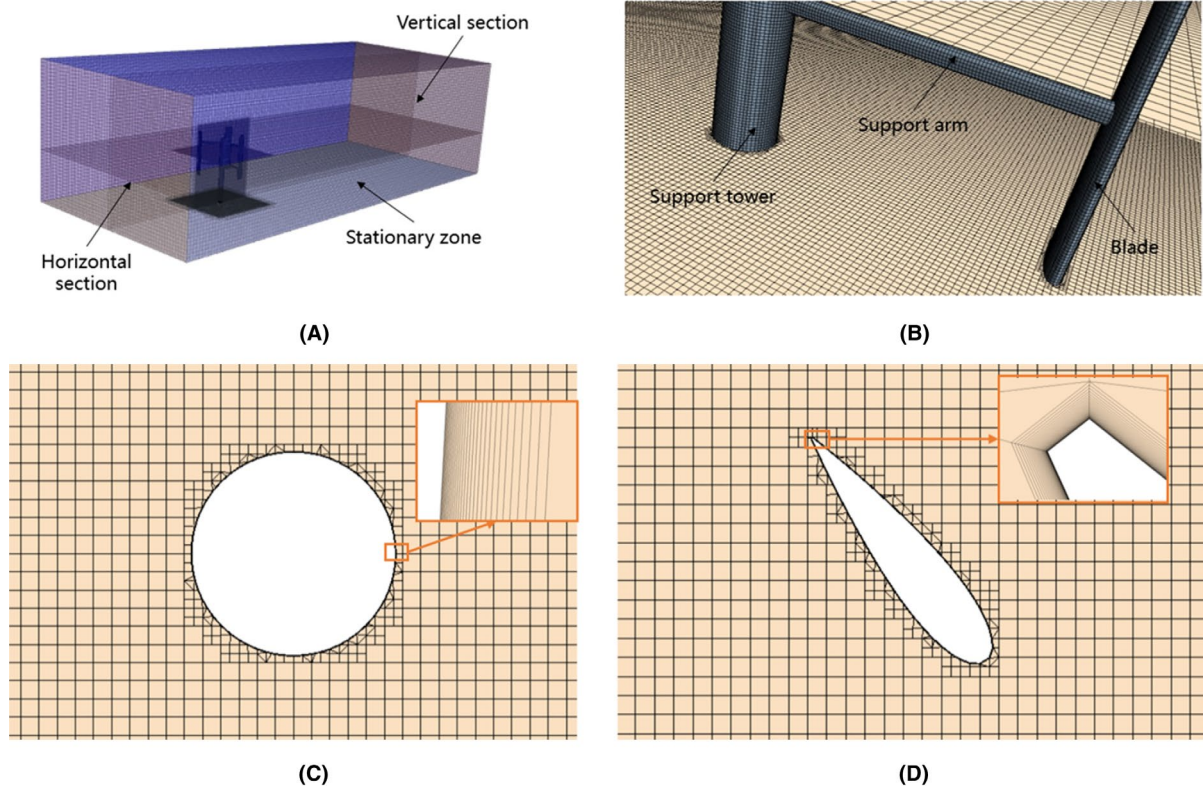
FIGURE 6 Mesh topology of the computational domain: A, over view of the grids; B, mesh topology around the VAWT; C, boundary layer grids of the support tower; D, boundary layer grids of the blade

5.1 | Surface pressure analysis

This section discusses the surface pressure of the VAWT in three steady wind conditions with $V_1 = 5$ m/s, $V_2 = 10$ m/s, and $V_3 = 20$ m/s, and the effects of different parked conditions on the pressure distribution of the structure are studied. The pressure distributions on the windward surface of the VAWT in the first parked condition at 20 seconds are presented in Figure 8. The results show that the contours of the pressure distribution are similar in different wind conditions and the pressure increases significantly as the wind velocity increases. It can be seen that the contours of the support tower are basically symmetrical along the z-axis which gradually change from positive pressure area to negative pressure area. For blade 2 (See Figure 3B), the larger positive pressure occurs in the mid-span parts near the trailing edge and the pressure decreases to 0.000 Pa or negative values at the other three edges; for blade 3, the larger positive pressure occurs at the two ends of the trailing edge and a smaller positive pressure occurs at the middle of the trailing edge; for blade 1, the maximum negative pressures appear at the right edge in all three conditions, which are −38.888 Pa, −175.390 Pa, and −729.210 Pa, respectively. It is also found from Figure 8 that the contours of the pressure distribution on the blade 2 are relatively regular while they are disorderly on blade 3. This is because blade 2 first interacts with the incoming flow, which affects the surface pressure of the subsequent structure while disturbing the flow field.

Meanwhile, there are some differences in the pressure distributions between the three wind conditions. As shown in Figure 8A,B, when the wind velocity is $V_1 = 5$ m/s and
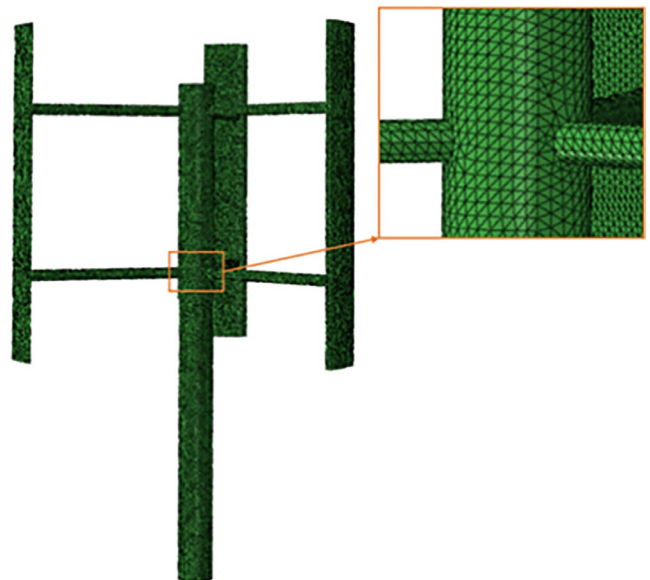
FIGURE 7 3D view of the finite element model of the VAWT

TABLE 2 Mesh independence test based on the relative errors of dynamic responses of the top section

Mesh type	Number of mesh	Maximum displacement (mm)	Relative error	Average displacement (mm)	Relative error	Maximum velocity (mm/s)	Relative error
Coarse	6 236 743	0.9012	−6.90%	0.2803	11.81%	8.926	−20.37%
Medium	7 871 364	0.9627	−0.55%	0.2348	−6.34%	11.600	3.48%
Fine	10 712 312	0.9680	–	0.2507	–	11.210	–

TABLE 3 Mesh independence test based on the relative errors of dynamic responses of the variable section

Mesh type	Number of mesh	Maximum displacement (mm)	Relative error	Average displacement (mm)	Relative error	Maximum velocity (mm/s)	Relative error
Coarse	6 236 743	0.4054	−5.06%	0.1227	13.40%	4.031	−18.93%
Medium	7 871 364	0.4267	−0.07%	0.1017	−6.01%	4.875	−1.95%
Fine	10 712 312	0.4270	–	0.1082	–	4.972	–

$V_2 = 10$ m/s, the maximum positive pressure appears in the middle of the two parts of the support tower, which is 16.891 Pa and 61.121 Pa, respectively. However, the maximum positive pressure only exists in the middle of the lower part of the support tower when the wind velocity is $V_3 = 20$ m/s (Figure 8C), which is 269.47 Pa. Besides, among the three wind conditions, when the wind velocity is 10 m/s, the area of the larger positive pressure on blade 2 is the biggest, while blade 3 is the smallest. The reason can be that the deformation of the VAWT gradually leads to changes in surface pressure.

Figure 9 shows the comparison of the surface pressure of the VAWT in three parked conditions at the velocity of 10 m/s. It can be seen that under the three parked conditions, the maximum and minimum values of the surface wind pressure are not much different. For the pressure distribution on blade 2 in the third parked condition (Figure 9C), the same result is found on blade 3 in the first parked condition (Figure 9A). However, there are subtle differences in the pressure distribution on the blades. For blade 1 in the second

parked condition (Figure 9B), the larger positive pressure occurs in the mid-span parts near the leading edge, rather than the trailing edge, which is different from the phenomenon that occurs in blade 2 under the first parked condition (Figure 9A).

5.2 | Flow characteristics analysis

The flow characteristics of the VAWT at different wind velocities with $V_1 = 5$ m/s, $V_2 = 10$ m/s, and $V_3 = 20$ m/s are discussed in this section. The differences between the flow field in three parked condition are analyzed. Figure 10 shows the vorticity magnitudes of the horizontal section ($z = 7.5$ m) and vertical section of the VAWT in the first parked condition at 20 seconds. The specific locations of the two sections are shown in Figure 6A. As shown in Figure 10A,C,F, the vorticity increases significantly as the height of the support tower increases, and the three-dimensional motion characteristics of the turbulent flow become more obvious. It also shows that as the wind velocity increases, the disturbance

TABLE 4 Time step test based on the relative errors of dynamic responses of the top section

Time step	Maximum displacement (mm)	Relative error	Average displacement (mm)	Relative error	Maximum velocity (mm/s)	Relative error
0.05 s	0.8998	−12.98%	0.2992	16.51%	8.401	−23.83%
0.01 s	0.9627	−6.90%	0.2348	−8.57%	11.600	5.17%
0.005 s	1.0340	–	0.2568	–	11.030	–

TABLE 5 Time step test based on the relative errors of dynamic responses of the variable section

Time step	Maximum displacement (mm)	Relative error	Average displacement (mm)	Relative error	Maximum velocity (mm/s)	Relative error
0.05 s	0.3832	−14.02%	0.1269	14.12%	3.609	−28.59%
0.01 s	0.4267	−4.26%	0.1017	−8.54%	4.875	−3.54%
0.005 s	0.4457	–	0.1112	–	5.054	–
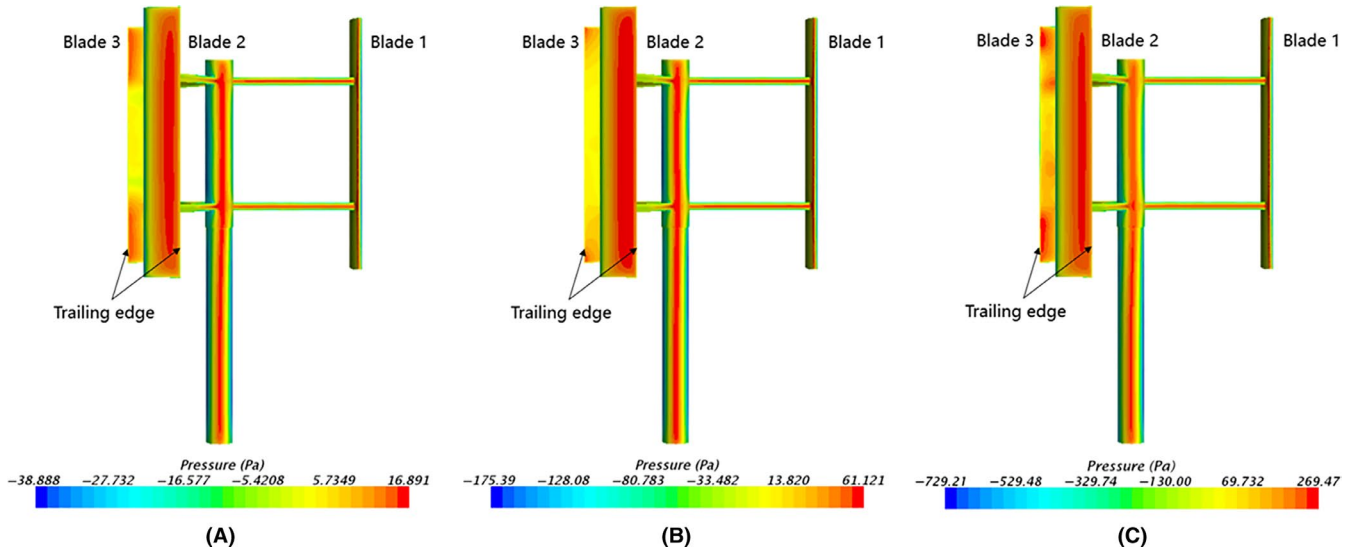
FIGURE 8 Contours of the instantaneous pressure distribution on the windward surface of the VAWT in the first parked condition: A, $V_1 = 5$ m/s; B, $V_2 = 10$ m/s; C, $V_3 = 20$ m/s
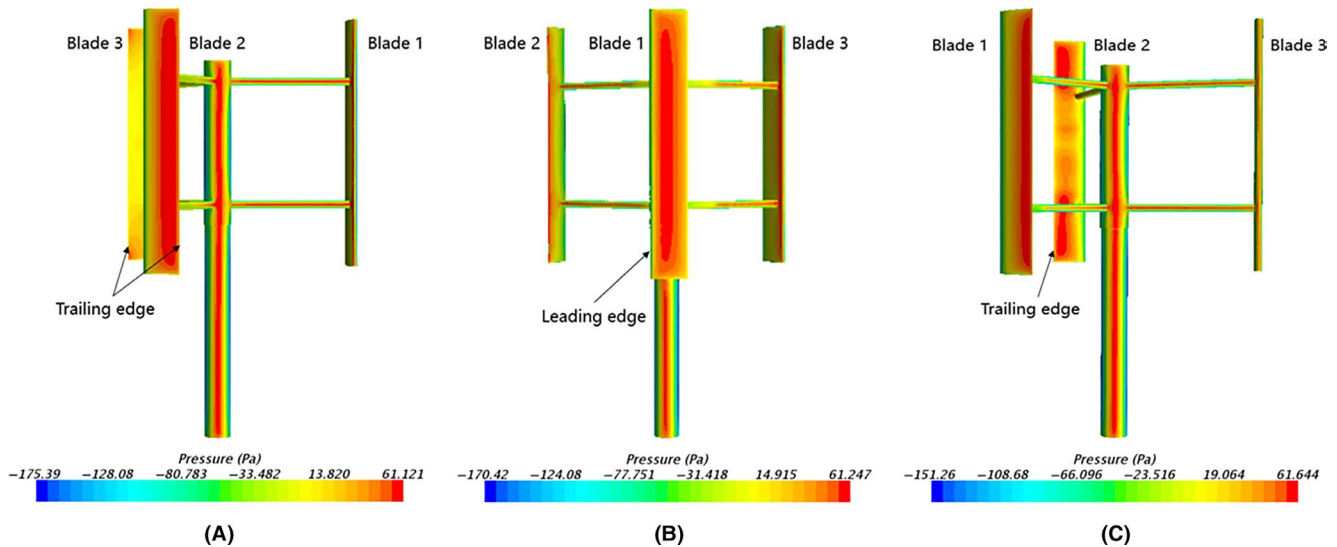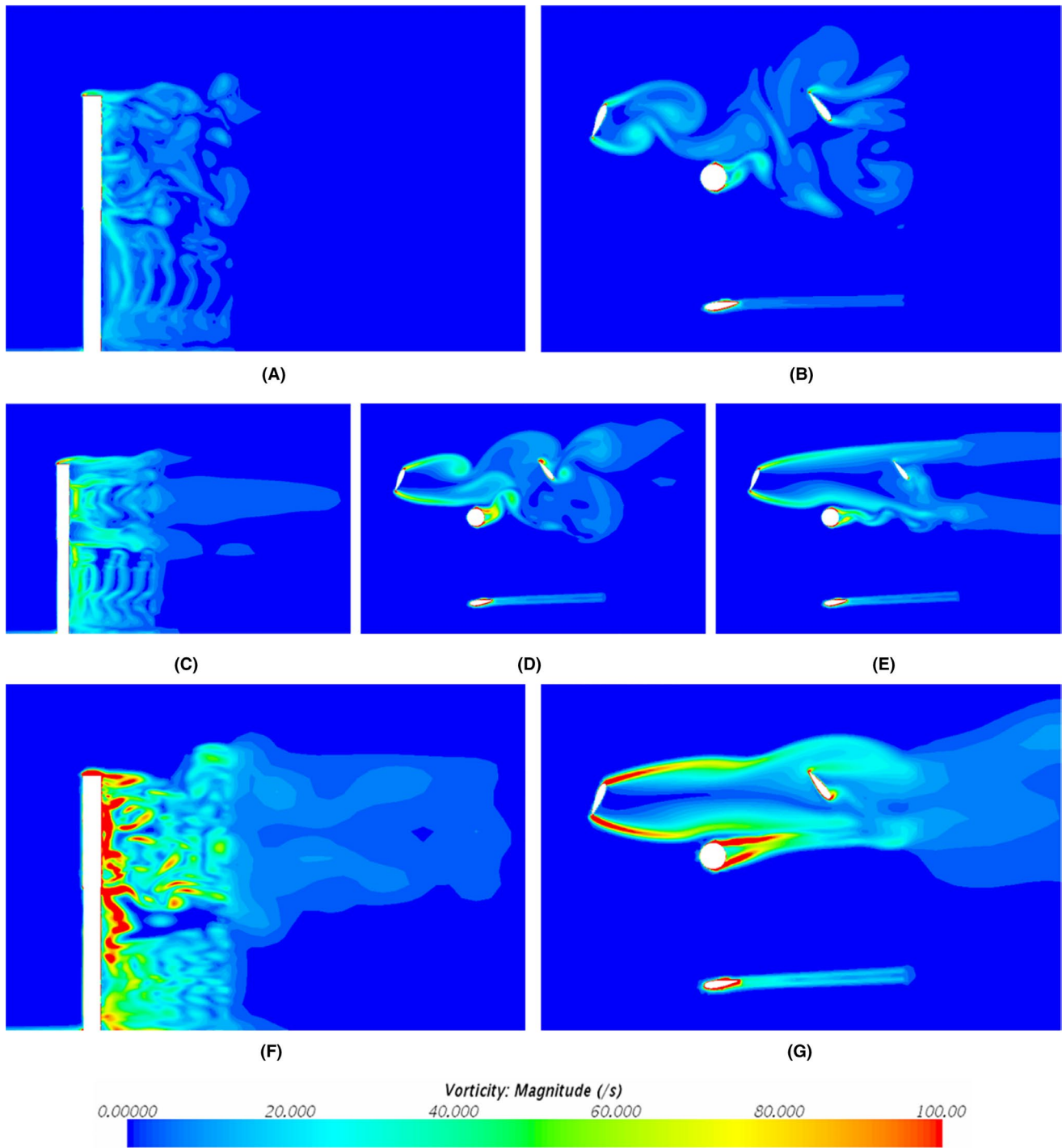

FIGURE 9 Contours of the instantaneous pressure distribution on the windward surface of the VAWT in three parked conditions at $V_2 = 10$ m/s: A, the first parked condition, $\theta = 0°$; B, the second parked condition, $\theta = 90°$; C, the third parked condition, $\theta = 135°$

range of the wake flow increases continuously which the same phenomenon is obtained in Figure 10B,E,G, the vorticity near the inner boundary layers of the support tower increases obviously while the vorticity does not change significantly in other areas of the flow field, and the vortices at the end of the flow field generate in an asymmetry way.

It can be seen from Figure 10B,E,G that the large vortex is not formed around the blade 1, the flow attaches to its surface and the flow separation does not appear. It is also clearly seen that the vortex structures around the blade 2 and blade 3 become very different when the wind velocity increases, and the vortices substantially disappear, where only two banded vortex structures are formed on the trailing edge and leading edge of the airfoil. This is because the

flow velocity of the flow field increases rapidly, and the vortex structure around the blade is taken away as soon as it develops. The specific process can be seen in Figure 10E,F. When the flow field has not been fully developed, a series of different magnitudes of vortices around the airfoil can be observed, the Karmen vortex street phenomenon behind the support tower is obvious, and its shedding vortices interact with the blade 3. However, the above phenomena no longer exist as the flow field develops completely.

Figure 11 shows the vorticity magnitudes of the horizontal and vertical sections of the VAWT in three parked conditions at the velocity of 10 m/s. From Figure 11A,C it can be seen that there is almost no difference in the flow field between the two conditions. In the second parked condition,
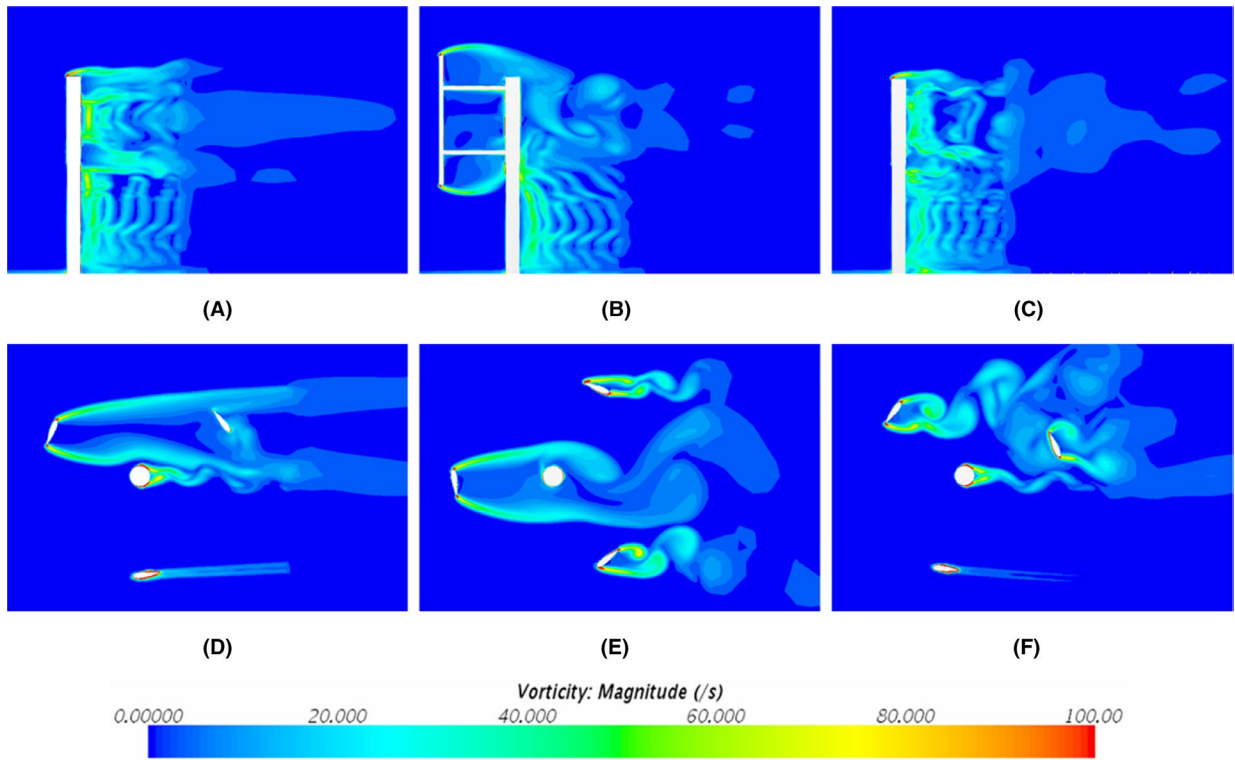
FIGURE 10 Instantaneous contours of vorticity magnitude of the VAWT at different wind velocities: A, B, $V_1 = 5$ m/s; C, D, E, $V_2 = 10$ m/s; F, G, $V_3 = 20$ m/s

the vorticity intensity near the inner boundary layers of the upper part support tower is significantly reduced due to the blades and support arms interfering with the incoming flow. It is found in Figure 11E that the phenomenon of the Karmen vortex street does not appear behind the support tower due to the fully developed wake disturbance of blade 1. In addition, the vortex structures around the airfoil in the second and third parked conditions are more abundant than the first

one, indicating that the slight difference in the position of the blade relative to the incoming flow will result in a large change in the flow field.
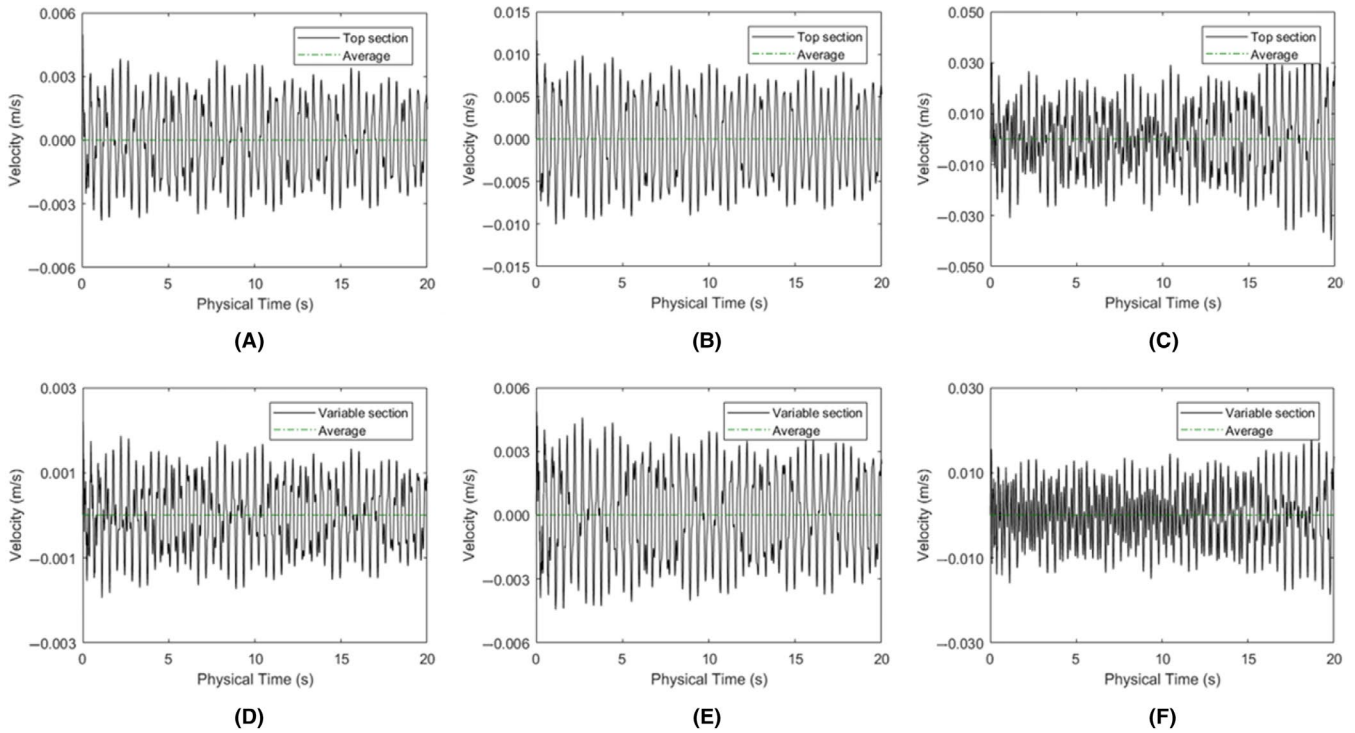
5.3 | Dynamic responses analysis

In this section, the dynamic responses of the VAWT in three steady wind conditions are discussed. The effects of different

FIGURE 11 Instantaneous contours of vorticity magnitude of the VAWT in three parked conditions at $V_2 = 10$ m/s: A, D, the first parked condition, $\theta = 0°$; B, E, the second parked condition, $\theta = 90°$; C, F, the third parked condition, $\theta = 135°$
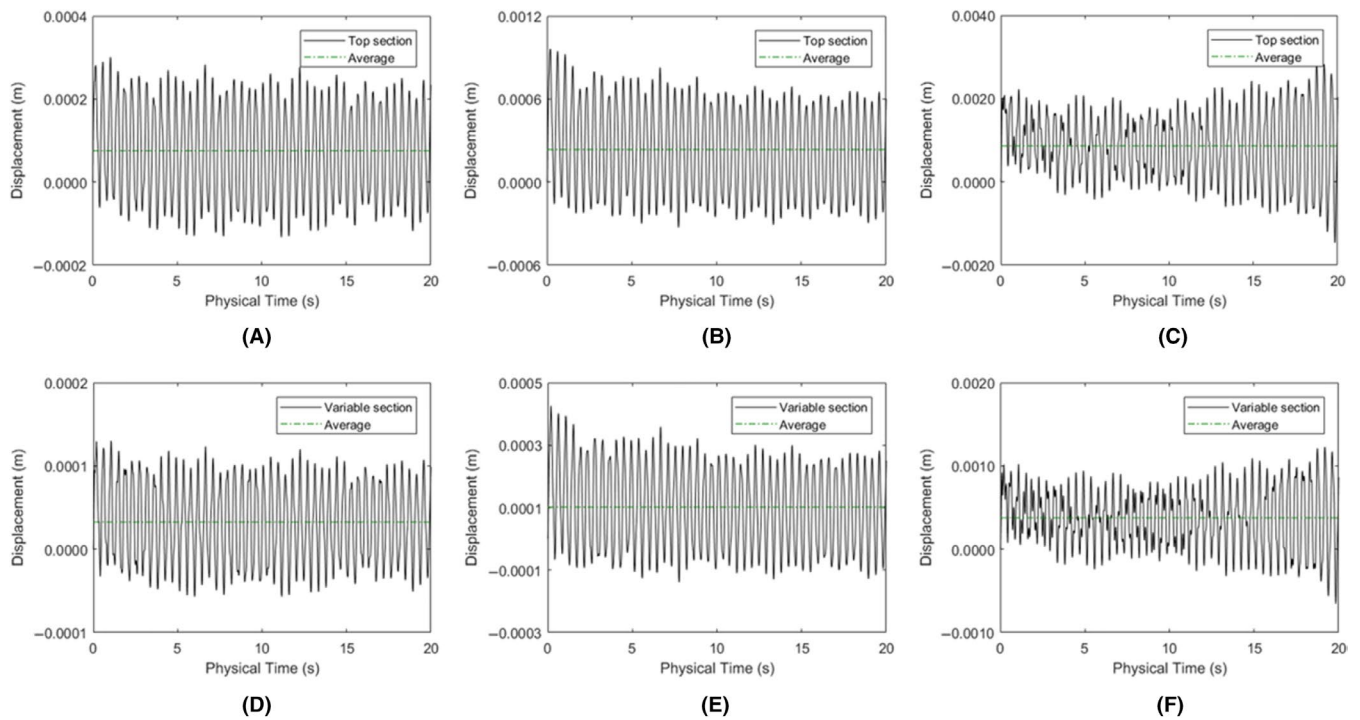
FIGURE 12 Displacement responses in the x-direction at critical sections of the support tower in the first parked condition: A, D, $V_1 = 5$ m/s; B, E, $V_2 = 10$ m/s; C, F, $V_3 = 20$ m/s

FIGURE 13 Velocity responses in the *x*-direction at critical sections of the support tower in the first parked condition: A, D, $V_1 = 5$ m/s; B, E, $V_2 = 10$ m/s; C, F, $V_3 = 20$ m/s

parked conditions on the dynamic responses of the structure are also analyzed. Besides, the dynamic behaviors of some critical sections of the support tower, blades, and support arms are compared. The top section ($z = 9.6$ m) and variable section ($z = 5.4$ m) of the support tower, the top section ($z = 10.65$ m) and bottom section ($z = 4.35$ m) of the blades, and the mid-span part ($z = 5.925$ m, 9.075 m) of the support arms are selected as the research objects. The specific locations of the critical sections are shown in Figure 4A. The time-domain displacement and velocity responses of the above structural components in the *x*-direction (Figure 4) under three parked conditions are calculated at different wind velocities, where $V_1 = 5$ m/s, $V_2 = 10$ m/s and $V_3 = 20$ m/s.

Figures 12 and 13 show the displacement and velocity responses of the support tower in the first parked condition, respectively. The representative dynamic responses data are given in Table 6. It can be seen that in all three wind conditions, the displacements have certain periodicity and fluctuate around different average values, and the velocity curves also fluctuate steadily around 0.000 m/s. The similar result for the displacement is obtained in the research of Wang et al[27] It shows that the support tower reaches a new forced vibration equilibrium state from the free vibration equilibrium state under wind loads. It is also found in Table 6 that the displacement and velocity at the top section are relatively 2.5 times than those of the variable section, which is consistent with the theory of structural mechanics. Meanwhile, it is obvious that as the wind velocity increases, the dynamic responses of the support tower increase significantly, affecting the structural safety of the VAWT.

The dynamic responses of the blades and support arms in the first parked condition at $V_3 = 20$ m/s are given in Figures 14 and 15, respectively. It can be seen from the two figures that the displacement and velocity of the blades

TABLE 6 Representative dynamic responses data of the support tower in the first parked condition

| Wind velocity	5 m/s		10 m/s		20 m/s	
Position	Top section	Variable section	Top section	Variable section	Top section	Variable section
Displacement (maximum) (mm)	0.3009	0.1304	0.9627	0.4267	2.8610	1.2290
Displacement (average) (mm)	0.07558	0.03270	0.23480	0.10170	0.86640	0.37620
Velocity (maximum) (mm/s)	4.976	2.203	11.600	4.875	39.770	18.890
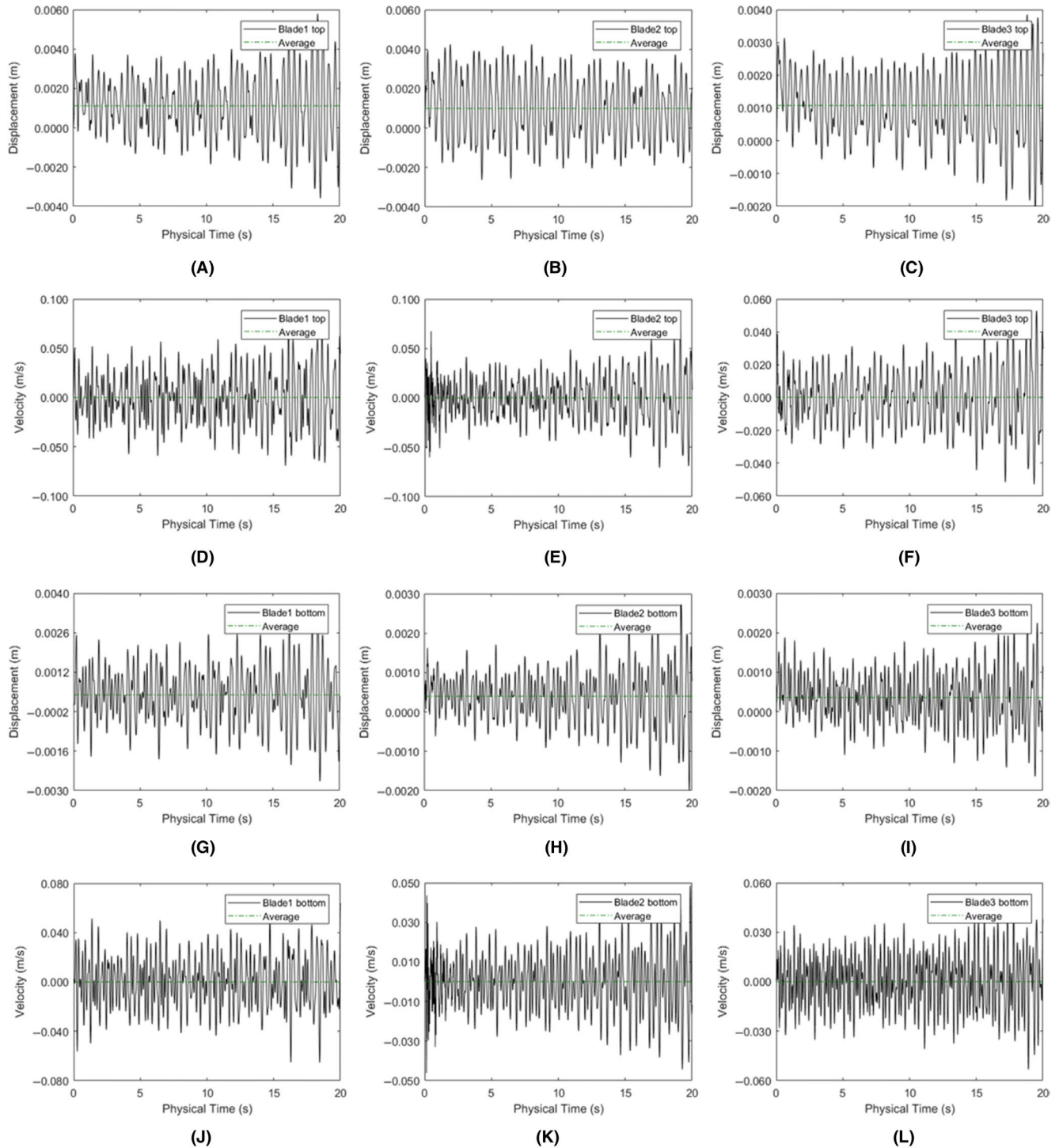
FIGURE 14 Displacement and velocity responses in the *x*-direction at critical sections of the blades in the first parked condition under $V_3 = 20$ m/s: A, B, C, displacement of the blade top section; D, E, F, velocity of the blade top section; G, H, I, displacement of the blade bottom section; J, K, L, velocity of the blade bottom section

and support arms are substantially larger than that of the support tower. For the blades, the reason can be that the material of the blade is aluminum alloy, and its density and elastic modulus are rather smaller than the steel. As for the support arms, its diameter is small, resulting in less rigidity. Besides, the contact area between the two components

is small, and the structural performance is not ideal. These indicate that the blades and support arms deserve more attention whether its deformation meets the regular service requirements of the VAWT.

Figure 14 shows that the dynamic responses of the blade top section are more obvious than that of the bottom section
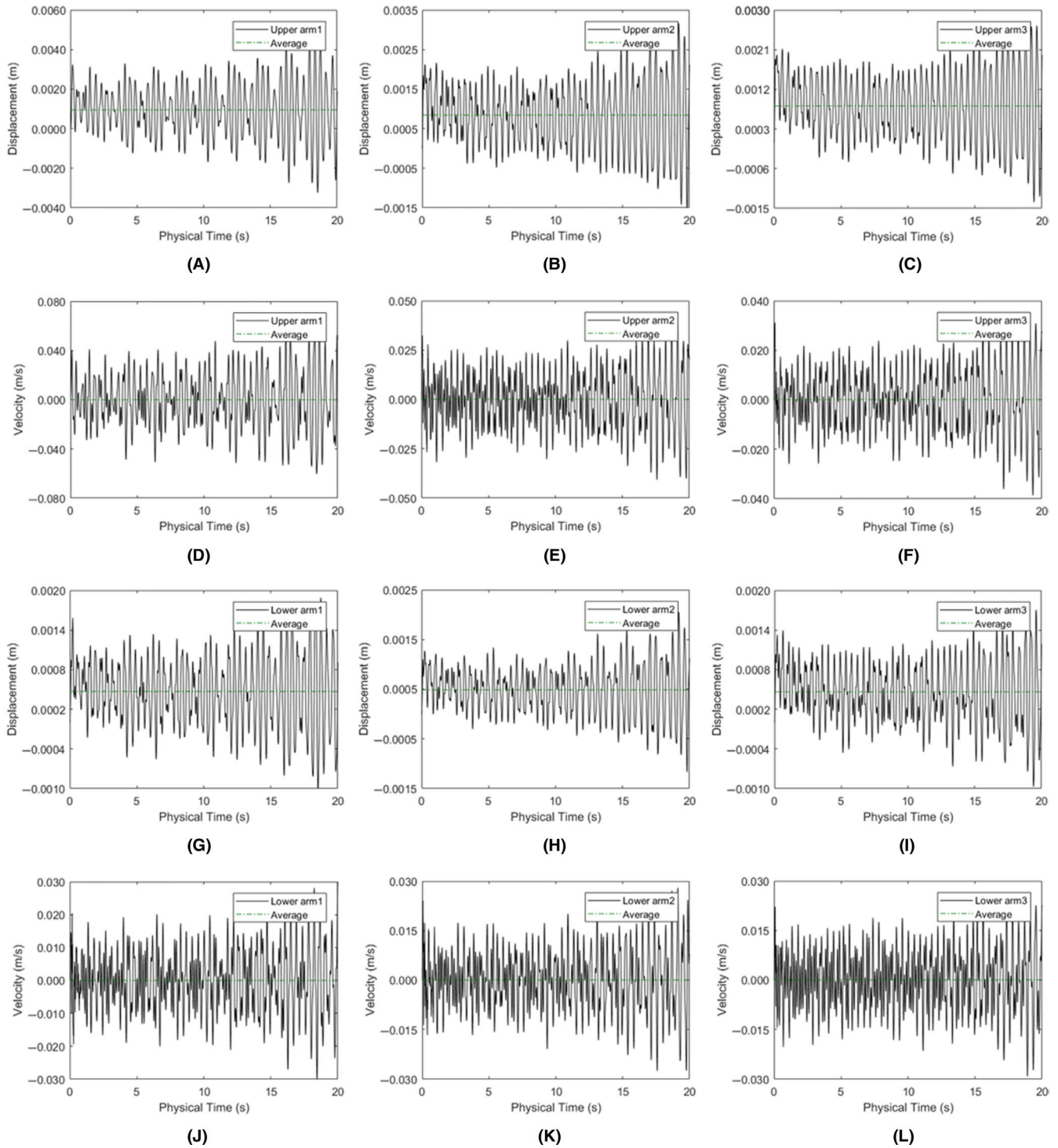
FIGURE 15 Displacement and velocity responses in the *x*-direction at mid-span parts of the support arms in the first parked condition under $V_3 = 20$ m/s: A, B, C, displacement of the upper arm; D, E, F, velocity of the upper arm; G, H, I, displacement of the lower arm; J, K, L, velocity of the lower arm

and blade 1 vibrates most intensely. It is also found in Figure 15 that the deformation of the upper arm is larger than the lower arm, and arm 1 has the most severe vibration. Combined with the flow characteristics and surface pressure distribution of the VAWT in the first parked condition, the reason can be that blade 1 and arm 1 first interact with the incoming flow and disturb the

flow field, so that the surface pressure of blade 3 and arm 3 is reduced, resulting in a decrease in the dynamic responses.

Table 7 shows the comparison of the dynamic responses of the VAWT support tower under three parked conditions at the velocity of 10 m/s. It can be seen that the average displacement and maximum velocity of the support tower are

TABLE 7 Comparison of the representative dynamic responses data of the support tower in three parked conditions under $V_2 = 10$ m/s

Wind velocity	10 m/s					
Parked condition	First		Second		Third	
Position	Top section	Variable section	Top section	Variable section	Top section	Variable section
Displacement (maximum) (mm)	0.9627	0.4267	0.9290	0.4028	0.9759	0.4225
Displacement (average) (mm)	0.23480	0.10170	0.26100	0.11170	0.28160	0.12190
Velocity (maximum) (mm/s)	11.600	4.875	11.910	6.328	11.870	5.393

smallest in the first parked condition. For the third parked condition, the average displacement of the support tower is significantly larger than that of the first and second conditions. However, considering that the deformations of the support tower in the three conditions are much smaller than the limiting value under regular service, the effect of the parked condition on the dynamic responses of the VAWT can be neglected.

6 | CONCLUSIONS

This study mainly investigates the surface pressure distribution, flow characteristics, and dynamic responses of a straight-bladed VAWT in different steady wind conditions and different parked conditions by combining CFD and FEA techniques. Although the computational cost of the two-way coupling between STAR-CCM+ and ABAQUS is high, it can capture the deformation and surrounding flow of the VAWT simultaneously and accurately. The main conclusions are as follows.

1. The contours of the pressure distribution on the windward surface of the VAWT are similar under a few different conditions and the pressure increases significantly as the wind velocity increases. The distribution of the surface pressure on blades shows a certain regularity. The interaction between the blade and flows affects the pressure distribution of the subsequent structure. The deformation of the VAWT leads to changes in the maximum positive pressure distribution on the support tower. The maximum and minimum values of the surface wind pressure are not much different in different parked conditions.

2. The three-dimensional motion characteristics of the turbulent flow and the turbulent effect of the wake flow become more obvious as the wind velocity increases. Meanwhile, the vortex structures of the airfoils change significantly which may have an impact on the dynamic responses of the VAWT. The slight difference in the position of the

blade relative to the incoming flow will result in a large change in the flow field.

3. The VAWT works normally at a certain position under wind action, accompanied by the vibration. Due to the large displacement and velocity, the blades and support arms deserve more attention during the design to ensure the structural safety of the VAWT. The effects of the parked condition on the dynamic responses of the VAWT can be neglected.

In future works, the buckling stability and fatigue damage effect of the VAWT would be analyzed; more complicated working conditions would be considered which include fluctuating wind action and wind turbine rotation.

ORCID

Zhaolong Han https://orcid.org/0000-0002-6494-150X

Zhiyu Jiang 🔟 https://orcid.org/0000-0002-8778-0999

REFERENCES

1. Tummala A, Velamati RK, Sinha DK, Indraja V, Krishna VH. A review on small scale wind turbines. *Renew Sustain Energy Rev*. 2016;56:1351-1371.
2. Bhutta M, Hayat N, Farooq AU, Ali Z, Jamil SR, Hussain Z. Vertical axis wind turbine-a review of various configurations and design techniques. *Renew Sustain Energy Rev*. 2012;16:1926-1939.
3. Lei H, Zhou D, Bao Y, Li Y, Han Z. Three-dimensional improved delayed detached eddy simulation of a two-bladed vertical axis wind turbine. *Energy Convers Manage*. 2017;133:235-248.
4. Ismail MF, Vijayaraghavan K. The effects of aerofoil profile modification on a vertical axis wind turbine performance. *Energy*. 2015;80:20-31.
5. Ma N, Lei H, Han Z, et al. Airfoil optimization to improve power performance of a high-solidity vertical axis wind turbine at a moderate tip speed ratio. *Energy*. 2018;150:236-252.
6. Jacob J, Chatterjee D. Design methodology of hybrid turbine towards better extraction of wind energy. *Renewable Energy*. 2019;131:625-643.
7. Lin J, Leung L, Xu Y, Zhan S, Zhu S. Field measurement, model updating, and response prediction of a large-scale straight-bladed vertical axis wind turbine structure. *Measurement*. 2018;130:57-70.
8. Nguyen L, Metzger M. Optimization of a vertical axis wind turbine for application in an urban/suburban area. *J Renew Sustain Energy*. 2017;9(4):043302.
9. Tjiu W, Marnoto T, Mat S, Ruslan MH, Sopian K. Darrieus vertical axis wind turbine for power generation II: challenges in HAWT and the opportunity of multi-megawatt Darrieus VAWT development. *Renewable Energy*. 2015;75:560-571.
10. Lei H, Zhou D, Bao Y, Chen C, Ma N, Han Z. Numerical simulations of the unsteady aerodynamics of a floating vertical axis wind turbine in surge motion. *Energy*. 2017;127:1-17.
11. Li Q, Maeda T, Kamada Y, Murata J, Furukawa K, Yamamoto M. Effect of number of blades on aerodynamic forces on a straight-bladed Vertical Axis Wind Turbine. *Energy*. 2015;90:784-795.
12. Wang Y, Lu W, Dai K, Yuan M, Chen S. Dynamic study of a rooftop vertical axis wind turbine tower based on an automated vibration data processing algorithm. *Energies*. 2018;11(11):3135.
13. Mclaren K, Tullis S, Ziada S. Measurement of high solidity vertical axis wind turbine aerodynamic loads under high vibration response conditions. *J Fluids Struct*. 2012;32:12-26.
14. Mabrouk IB, Hami EA. Dynamic response analysis of Darrieus wind turbine geared transmission system with unsteady wind inflow. *Renewable Energy*. 2018;43:482-493.
15. Rebelo C, Veljkovic M, da Silva LS, Simoes R, Henriques J. Structural monitoring of a wind turbine steel tower-Part I: system description and calibration. *Wind Struct*. 2012;15:285-299.
16. Avila SM, Shzu M, Pereira WM, Morais M, Prado Z. Numerical modeling of the dynamic behavior of a wind turbine tower. *J Vib Eng Technol*. 2016;4(3):249-257.
17. Li C, Yu A, Li J, Xiang B, Peec-Org C. Dynamic analysis of vertical-axis wind turbines under the rotation. *Power and Energy Engineering Conference*. 2010;2010:634-638.
18. Feliciano J, Cortina G, Spear A, Calaf M. Generalized analytical displacement model for wind turbine towers under aerodynamic loading. *J Wind Eng Ind Aerodyn*. 2018;176:120-130.
19. Shi F, Wang Z, Zhang J, Gong Z, Guo L. Influences of wind and rotating speed on the fluid-structure interaction vibration for the offshore wind turbine blade. *J Vibroeng*. 2019;21(2):483-497.
20. Sorensen JN. Aerodynamic aspects of wind energy conversion. *Annu Rev Fluid Mech*. 2011;43:427-448.
21. Posa A, Parker CM, Leftwich MC, Balaras E. Wake structure of a single vertical axis wind turbine. *Int J Heat Fluid Flow*. 2016;61:75-84.
22. Bazilevs Y, Korobenko A, Deng X, Yan J, Kinzel M, Dabiri JO. Fluid-structure interaction modeling of vertical-axis wind turbines. *J Appl Mech-Trans ASME*. 2014;81(8):081006.
23. Menter FR. Two-equation eddy-viscosity turbulence models for engineering applications. *AIAA J*. 1994;32(8):1598-1605.
24. Newmark NM. A method of computation for structural dynamics. *J Eng Mech, ASCE*. 1959;85:67-94.
25. Glück M, Breuer M, Durst F, Halfmann A, Rank E. Computation of fluid-structure interaction on lightweight structures. *J Wind Eng Ind Aerodyn*. 2001;89:1351-1368.
26. Su J, Lei H, Zhou D, et al. Aerodynamic noise assessment for a vertical axis wind turbine using Improved Delayed Detached Eddy Simulation. *Renewable Energy*. 2019;141:559-569.
27. Wang Z, Zhao Y, Li F, Jiang J. Extreme dynamic responses of MW-level wind turbine tower in the strong typhoon considering wind-rain loads. *Math Problems Eng*. 2013;2013:1-13.